Materials Chemistry and Physics 270 (2021) 124800

Contents lists available at ScienceDirect

Materials Chemistry and Physics

journal homepage: www.elsevier.com/locate/matchemphys

High-temperature sliding wear behavior of nitrided $Ni_{45}(CoCrFe)_{40}(AlTi)_{15}$ high-entropy alloys

L.W. Lan [a], H.J. Yang [a,*], R.P. Guo [a], X.J. Wang [a], M. Zhang [a], P.K. Liaw [b], J.W. Qiao [a,**]

[a] College of Materials Science and Engineering, Taiyuan University of Technology, Taiyuan 030024, China
[b] Department of Materials Science and Engineering, The University of Tennessee, Knoxville 37996, USA

HIGHLIGHTS

- Hard particles of AlN, CrN, Fe_4N, and TiN phases were produced after nitriding.
- The surface hardness of HEAs increased from 8.8 GPa to 14.9 GPa after nitriding.
- The thickness of the nitrided layer on $Ni_{45}(FeCoCr)_{40}(AlTi)_{15}$ HEAs was 11.5 μm.
- The wear resistance of nitrided HEAs was superior than that of as-cast HEAs.
- Oxidative behavior played a dominant role in high wear resistance of HEAs.

GRAPHICAL ABSTRACT

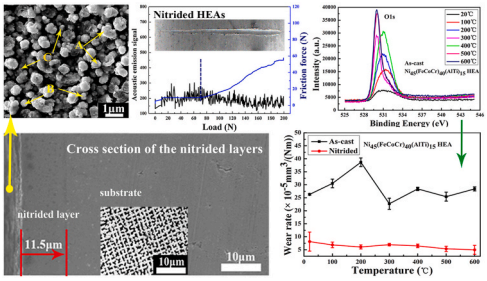

ARTICLE INFO

Keywords:
Microstructure
Oxidation
Friction
Wear

ABSTRACT

The nitrided layer on $Ni_{45}(CoCrFe)_{40}(AlTi)_{15}$ high-entropy alloys (HEAs) was prepared by plasma nitriding. The microstructure, hardness, the effect of temperature on the tribological properties and adhesive strength of the nitride layer were investigated. The results revealed that the as-cast alloy was composed of a single FCC phase, and the hardness measured by nano-indentation was 8.8 GPa. After nitriding, the hard phases, such as AlN, CrN, Fe_3N, and TiN, appeared, the surface hardness was increased to 14.9 GPa, and the hardness distribution of the cross section of the nitrided layer was uniform. Moreover, the scratch test showed that the nitrided layer had good bonding properties with the substrate. The friction coefficient and the wear rate were significantly reduced, compared to the as-cast alloys due to the generation of unique nitride particles on the surface of the nitrided alloys. At low temperatures, the friction mechanism of as-cast and nitrided alloys was dominated by the adhesive wear and abrasive wear. Subsequently, the friction mechanism was changed to the oxidative wear and delamination wear with increasing the temperature.

1. Introduction

The high-entropy alloys (HEAs) are composed of five or more metals with the same atomic ratio or near atomic ratio between 5 and 35 at.% of the main alloy elements [1]. Due to their high mixing entropy, these alloys tend to form a stable and simple single-phase structures, such as face-centered-cubic (FCC), body-centered-cubic (BCC), and/or hexagonal-closed-packed (HCP) rather than complex intermetallic

* Corresponding author
** Corresponding author
E-mail addresses: pineyang@126.com (H.J. Yang), qiaojunwei@gmail.com (J.W. Qiao).

https://doi.org/10.1016/j.matchemphys.2021.124800
Received 17 December 2020; Received in revised form 28 May 2021; Accepted 1 June 2021
Available online 3 June 2021

compounds [2,3]. These alloys usually cause the lattice distortion due to the different atomic size and chemical bonds of the constituent elements. Therefore, HEAs are stronger than conventional alloys [4,5]. Another key feature is the sluggish diffusion observed in HEAs [5,6], which is important for high-temperature applications because it means that the phases present have good high-temperature mechanical properties, which are usually controlled by diffusion dynamics [6,7].

According to the surveys conducted in different countries, the economic losses caused by friction and wear are estimated to be 1–2% of the Gross Domestic Product (GDP) [8]. The tribological properties of HEAs have become a hot topic due to their great potential in industrial applications [9–15]. Chuang et al. [12] designed a series of $Al_xCo_{1.5}CrFeNi_{1.5}Ti_y$ HEAs, and the wear behavior and mechanism were studied. The hard-phase η precipitation was suppressed due to the addition of Al, and the hardness was reduced from 509 HV of Al00Ti05 to 487 HV of Al02Ti05. However, when the molar ratio of Ti increased from 0.5 to 1 (Al00Ti10 and Al02Ti10), the volume fraction of η precipitates increased significantly, and the hardness was 654 H V and 717 H V. Therefore, the wear resistance was significantly improved.

The surface-coating technologies have been successfully applied to improve the surface hardness and tribological properties of metals and alloys. Researchers used ion implantation, Physical Vapor Deposition (PVD) technologies, to modify the surface of alloys [16–18]. However, the bonding strength or toughness of the modified layer was insufficient, which made it easy to crack and peel off under the bearing condition. Researchers have applied surface chemical heat treatment to high-entropy alloys to improve surface properties, such as boronizing and carburizing. The surface chemical heat treatment technologies have been applied to improve the surface properties of high-entropy alloys, such as the boronizing and carburizing [19–21]. However, the plasma nitriding is essentially a diffusion process different from other coating techniques. It is an excellent surface-hardening technique extensively used by the industry due to its high nitrogen potential, short processing time, and low environmental impact, improving the wear resistance, fatigue life, and corrosion resistance of parts, such as cams, gears, or molds, especially the parts containing the elements which have good binding ability with N, such as Al, Fe and Cr [22–25]. Nishimoto et al. [26] studied the microstructures and mechanical properties of CoCrFeMnNi HEAs. The results indicated that the FCC structure of the nitrided surface at lower nitriding temperatures was replaced by CrN at higher temperatures, and the surface hardness was increased from 200 HV of as-cast alloy to 1300 HV after nitriding, which greatly improved the wear resistance of the sample. Wang et al. [27] investigated the microstructures and wear properties of nitrided coatings on AlCoCrFeNi in different environments. It was concluded that the hardness of the nitrided HEA was significantly improved, compared to that of the as-cast alloy according to several strengthening mechanisms. The primary wear mechanism of the as-cast alloys in air was the abrasive wear, while the wear mechanism of the nitrided HEAs in the acid rain was oxidative and corrosive wears.

High-temperature wear is one of the limiting factors for the repeated contact-surface life of metals, and it is a potential failure mechanism for forging tools. Except for some refractory HEAs containing high melting point elements, the HEAs generally have the potential for high-temperature applications owing to their good oxidation resistance, superior age-softening resistance, and high elevated-temperature strengths [1,28,29]. The above reports were more concerned with the friction and wear properties of the nitride layer on HEAs at room temperature. However, the sliding-wear behavior for that at elevated temperature has so far rarely been investigated.

In the present study, the definition of traditional HEAs was broken through. The content of Ni was increased to 45 at.%. The configurational entropy of the alloy was 1.56 R higher than the defined value (1.5 R). Therefore, it still belonged to the category of HEAs. Previous study [30] showed that the as-cast $Ni_{45}(CoCrFe)_{40}(AlTi)_{15}$ HEAs had high yield strength ($\sigma_{0.2}$ = 1110 MPa) and great ductility (no fracture). However, the tribological behavior of the high entropy alloy was not clear. Therefore, the effects of temperature on the tribological properties of $Ni_{45}(CoCrFe)_{40}(AlTi)_{15}$ nitrided layers were discussed in detail.

2. Experimental

Alloy ingots with a nominal composition of $Ni_{45}(FeCoCr)_{40}(AlTi)_{15}$ were prepared by arc-melting a mixture of pure elemental metals (purity > 99 wt%, weight percent) in a Ti-gettered high-purity argon atmosphere with a water-cooled copper mold (WK-II Vacuum Arc Melter, China, manufactured by Beijing Wuke Optoelectronics Technology Co., Ltd.). These ingots were remelted five times under a vacuum environment so as to ensure a chemical homogeneity. The homogeneous melt was then cast into a water-cooled copper mold with a size of 85 (length) × 10 (width) × 2 mm (thickness).

In order to reduce the material waste caused by severe edge effects during the nitriding process, the entirely cuboid sample was carefully ground and fully polished. Subsequently, the plasma nitriding furnace (LDMC-100A, Germany) was used to perform the surface nitriding treatment on the polished samples in an ammonia atmosphere at 550 °C for 9 h. The flow rate of ammonia was 0.4 m^3/h. After nitriding, all the samples were cut into small pieces with a size of 10 (length) × 10 (width) × 1.5 mm (thickness).

The dry sliding-wear test was performed, using a universal wear-testing machine (HT-4001, China, manufactured by Lanzhou Institute of Chemical and Physics, Chinese Academy of Sciences) at different temperatures, such as 20, 100, 200, 300, 400, 500, and 600 °C, as schematically illustrated in Fig. 1. The temperature was recorded, employing the cromel-alumel thermocouples with the accuracy of ±1.5%. In order to avoid the experimental error due to the influence of temperature on the grinding pair, the tested samples were rubbed against a hardened Si_3N_4 ball with a diameter of 5.5 mm, at a distance of 8 mm from the center, a sliding velocity of 0.084 m/s (200 r/min) for 30 min, and a normal load of 10 N.

A load cell was used to record the friction coefficient during the tests. The volume loss of the alloys was calculated by measuring the depth and width of the wear scars, using a three-dimensional (3D) surface profiler based on scanning the white light interferometry. The volumetric loss is defined by Refs. [31,32]:

$$\Delta V = Lh\,(3h^2 + 4b^2)/(6b) \tag{1}$$

Where ΔV is the volumetric loss, L is the perimeter of the wear ring, h and b are the depth and width of the wear scars, respectively. The wear rate is defined as follows [31,32]:

$$Wr = \Delta V/(SP) \tag{2}$$

Where Wr is the wear rate, S is the sliding distance, and P is the load.

The microstructure and chemical composition of the alloys, the wear surface, and wear debris were analyzed, using a scanning electron

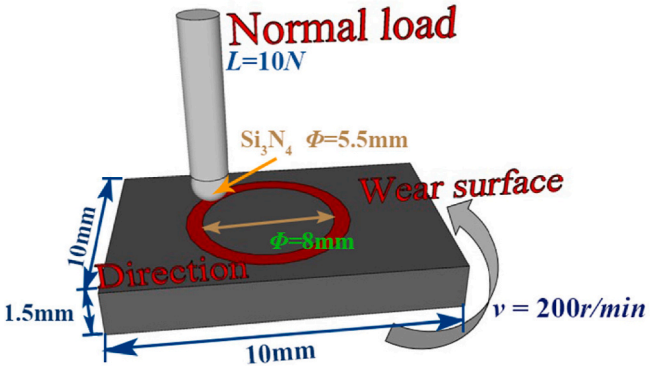

Fig. 1. Schematic diagram of a friction and wear test.

microscope (SEM, JEOLJSM-6390, Japan) with an attached X-ray energy-dispersive spectrometer (EDS, Oxford). The X-ray photoelectron spectroscopy analysis (XPS, K-Alpha, USA, Thermo Elemental) was used to determine the chemical compounds on the wear surfaces, and the nanoindentation test with Berkovich indenter (Nano Indenter G200, USA) was employed to measure the hardness of the surface and cross section of different samples. The displacement resolution was 0.01 nm, the strain rate was 0.05 s^{-1}, and the thermal drift rate was less than 0.5 nm/s. The crystal structure was characterized, using an X-ray diffractometer (XRD, D/MAX-2400, Japan, Rigaku) with the Cu Kα radiation. The scanning range was from 20° to 90° in 2θ at a scanning rate of 3°/min. The surface roughness was obtained by the atomic force microscope (FM-Nanoview 6600, China, manufactured by Zhengzhou Junyi Instrument Equipment Co., Ltd.). In addition, the scanning rate was 1 Hz and the scanning range was 400 × 400 nm. The scratch test was one of the most commonly-used methods to investigate the adhesion properties of engineering coatings. The scratch test was used to evaluate the adhesion strength between the nitride layer and substrate. The bonding strength of the nitrided layer was assessed using a microhardness tester equipped with an acoustic emission tester and a function recorder as a scratch tester. The load range was 0–200 N. The loading rate was 60 N/min, and the scratch speed was 2 mm/min.

3. Results

3.1. Phase and microstructure

Fig. 2 shows the XRD patterns of as-cast and nitrided $Ni_{45}(FeCoCr)_{40}(AlTi)_{15}$ HEAs. The diffraction peaks of the as-cast alloy are identified as a single FCC phase according to Fig. 2 (a). This structural feature was attributed to the high-entropy effect of HEAs, which indicated that (1) the high mixing entropy made the alloy system have a high degree of mixing, (2) the atoms of the alloy occupied the positions on the lattice sites randomly, and (3) the trend of atomic ordering and segregation decreased, inhibiting the formation of metal compounds and phase separation [1]. After nitriding, Fig. 2 (b) reflected that the intensity of the diffraction peak of the FCC phase decreased sharply. Furthermore, AlN, CrN, Fe_3N, and TiN phases were formed.

The as-cast microstructures and nitrided surface morphologies of $Ni_{45}(FeCoCr)_{40}(AlTi)_{15}$ HEAs are shown in Fig. 3. Typical cast dendrite and interdendrite structures (defined as DR and ID, respectively) are observed in the alloys. The chemical compositions of the different regions of the alloy analyzed by EDS are summarized in Table 1. The DR region is enriched in Al and Ni, but lack of Cr and Ti. On the contrary, Cr and Ti segregation are obviously seen in the ID region.

The initial surface roughness (Ra) of the mirror-polished specimens is 6.3 nm. After nitriding, the surface roughness (Ra) value increased to 97.7 nm due to the gas composition consisting of a greater amount of hydrogen, resulting in more sputtering and the formation of nitrides as observed by micro-particles on the surface [Fig. 3(b)]. The EDS analysis further confirmed the presence of nitrides in the form of microparticles, as presented in Table 2. These nanoparticles, smaller than 500 nm, are uniformly distributed on the nitrided surfaces of the $Ni_{45}(FeCoCr)_{40}(AlTi)_{15}$ HEAs. It is found that these large particles are the micro-aggregates of nanoparticles (The transformation from C to A). These results revealed that the nanoparticles of the nitrided layer aggregated and formed larger particles with increasing the nitriding temperature, resulting in the increase in the surface roughness. The formation of microaggregates was also confirmed by Wang et al. [33].

The results of the microstructure and elemental analysis of the cross section of the nitrided $Ni_{45}(FeCoCr)_{40}(AlTi)_{15}$ HEAs are shown in Fig. 4. A clear boundary is observed between the coating and the substrate (marked as the yellow dotted line), and the measured thickness of the nitride layer is 11.5 μm, which is also indicated by the EDS line-scanning results. The content of the N element remains stable, about 10 μm, after which a fast decrease occurs in a distance range about 1.5 μm, until the thickness of the nitrided layer reaches 11.5 μm. This trend suggests that the nitrided layer attained a high level of hardness. During the plasma nitriding, the element having lower entropy of formation with the N element tends to catch nitrogen atoms to form nitrides. As a result, the nitrogen concentration was saturated at a high level, forming nitrides. Moreover, the general variation in the nitrogen distribution is inverse to the typical variation of other metal elements throughout the distance range, including a rapid decrease in the distance from about 10 to 11.5 μm. Furthermore, the former variation is much larger than the latter. This trend is reasonable because the six elements of the alloy balance the change in the nitrogen content. Moreover, the EDS elemental mapping of the cross section of the nitride layer showed that the relative distributions of all metal elements in the nitrided layer and the matrix are substantially similar, while the N element of the nitrided layer is significantly richer than that in the matrix.

The matrix structure under the nitride layer is still a typical dendrite structure, and the dendrite and interdendrite are observed clearly.

Plasma nitriding is essentially a diffusion process different from other coating techniques. Various nitride compound layers may be produced on the surface but underneath the compound layer, there is a nitrogen-rich diffusion layer. The diffusion layer provides a strong support for the bonding between the nitrided layer and the substrate [34,35]. The scratch test is one of the most commonly-used methods to investigate the adhesion properties of engineering coatings. A scratch test was used to evaluate the adhesion strength between the nitride layer and substrate, which is shown in Fig. 5. The scratches appear deeper and wider with the load increasing from 0 to 200 N, which is fully reflected in Fig. 5(a) and (c). During this process, the increase in the friction force can be clearly divided into two stages: prior to about 72 N, the friction force remains stable, and after that, the friction force increases rapidly.

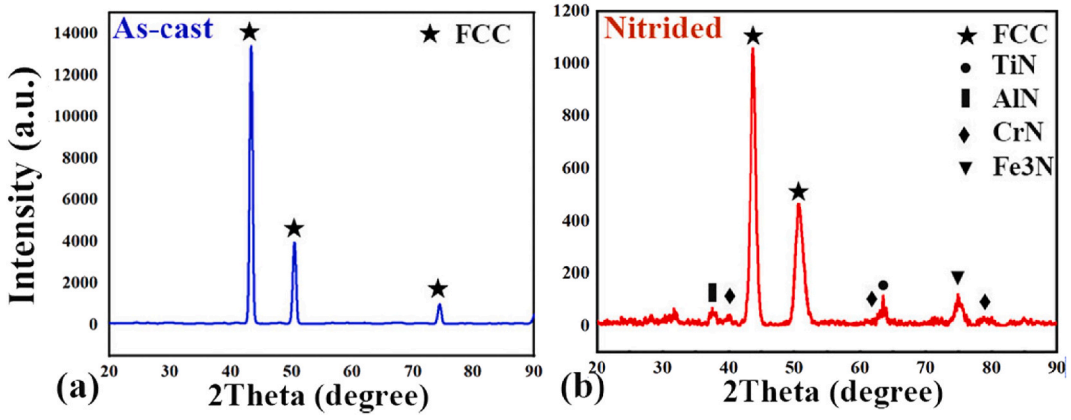

Fig. 2. XRD patterns of (a) as-cast and (b) nitrided $Ni_{45}(FeCoCr)_{40}(AlTi)_{15}$ HEAs.

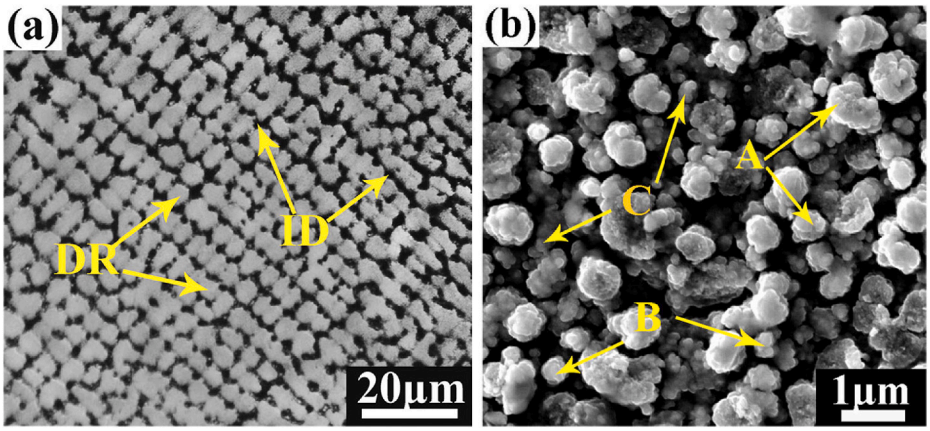

Fig. 3. SEM images for the microstructure of (a) as-cast and (b) nitrided $Ni_{45}(FeCoCr)_{40}(AlTi)_{15}$ HEAs.

Table 1
Chemical compositions of different regions in as-cast $Ni_{45}(FeCoCr)_{40}(AlTi)_{15}$ HEAs.

Composition (at. %)	Al	Co	Cr	Fe	Ni	Ti
DR	6.3	13.4	14.1	14	47.6	4.6
ID	2.3	12.2	19.3	12.2	41.7	12.4

Table 2
The elemental analysis of different forms of nitride particles in Fig. 2(b).

Composition (at. %)	Al	Co	Cr	Fe	Ni	Ti	N	O
A	7.0	5.6	4.9	18.4	14.4	3.1	20.8	25.8
B	6.2	4.0	9.0	16.5	14.8	3.9	15.8	29.7
C	6.6	6.4	8.7	23.4	14.8	4.0	8.0	19.6

Moreover, the depth of the detected scratch at this position is about 11.5 μm (the position marked by the blue dashed line in Fig. 5(a)), and the profile of the wear scar section is presented in Fig. 5(d). From this feature, it can be judged that the nitrided layer was penetrated with the load increasing to 72 N. In the process of loading and sliding, the acoustic-emission signal always fluctuates irregularly within a small range without mutation, which means that the nitrided layer was not destroyed. Large crack or brittle block spallation is not observed, indicating that the nitrided layer has good bonding properties with the substrate. The scanning morphologies showed that the two sides of the scratch surface are flat, and no trace of brittle peeling. In addition, the morphology of the scratch surface at the maximum deformation (Fig. 5 b) is clear and smooth without deep crack, indicating that the nitrided layer was not seriously damaged, which also verified the good bonding between the nitrided layer and the substrate. Moreover, the EDS line scan results from the N element showed that the thickness of the nitriding diffusion layer was 2 μm (from 9.5 to 11.5 μm), that is, the N element dropped from the beginning to the stable stage.

Fig. 6(a) displays the nano-hardness of the as-cast and nitrided alloys surfaces as a function of the indentation depth. It is concluded that the surface hardness of as-cast and nitrided alloys is 8.8 ± 0.2 GPa and 14.9 ± 0.2 GPa, respectively. The nitrided samples showed higher hardness with an increase by about a factor of 1.6, compared to that in the as-cast samples, which indicates that the nitrided alloys exhibited better performance in tribological applications. The hardness-depth profiles of as-cast and nitrided HEAs are presented in Fig. 6(b). The hardness of the as-cast samples at different depths is always maintained at 8.8 GPa with slight fluctuations, which is consistent with the surface hardness of the as-cast alloys. The hardness of the nitride layer at different depths from the surface is similar, about 14.9 GPa. However, the hardness decreases sharply near the interface between the nitride layer and the substrate until the hardness of the substrate under the nitride layer is 8.8 GPa, which is in line with the cross-sectional hardness of the as-cast sample. The stable nitride-layer hardness and uniform distribution of N elements indicate that a uniform and stable nitride layer with the high hardness is formed during the plasma-nitriding process, improving the wear resistance.

3.2. Wear behavior

3.2.1. Friction coefficient

Fig. 7 displays the variation of the friction coefficient of as-cast and nitrided $Ni_{45}(FeCoCr)_{40}(AlTi)_{15}$ HEAs with sliding times at different temperatures. The friction coefficient curves under different conditions

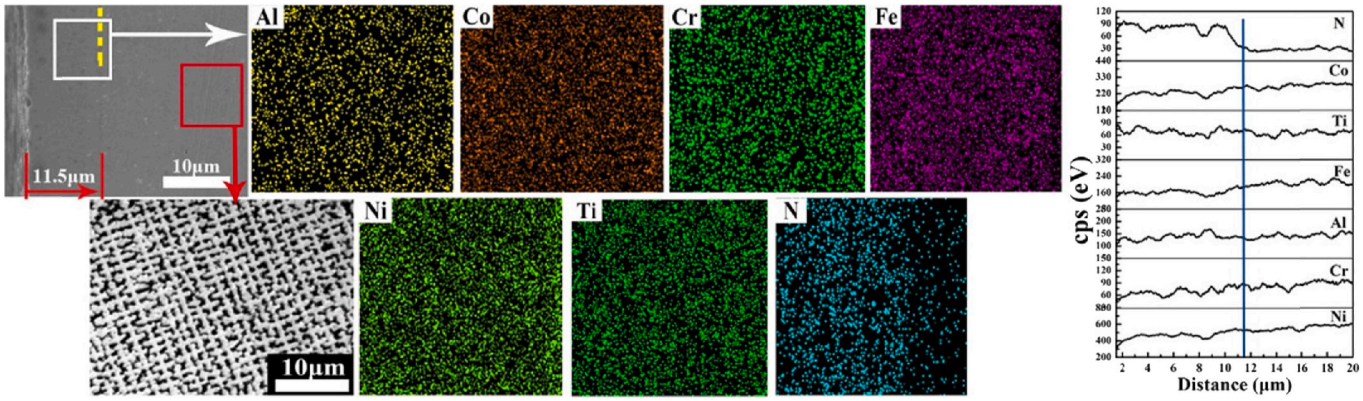

Fig. 4. The microstructure and elemental analysis of the cross section of the nitrided $Ni_{45}(FeCoCr)_{40}(AlTi)_{15}$ HEAs.

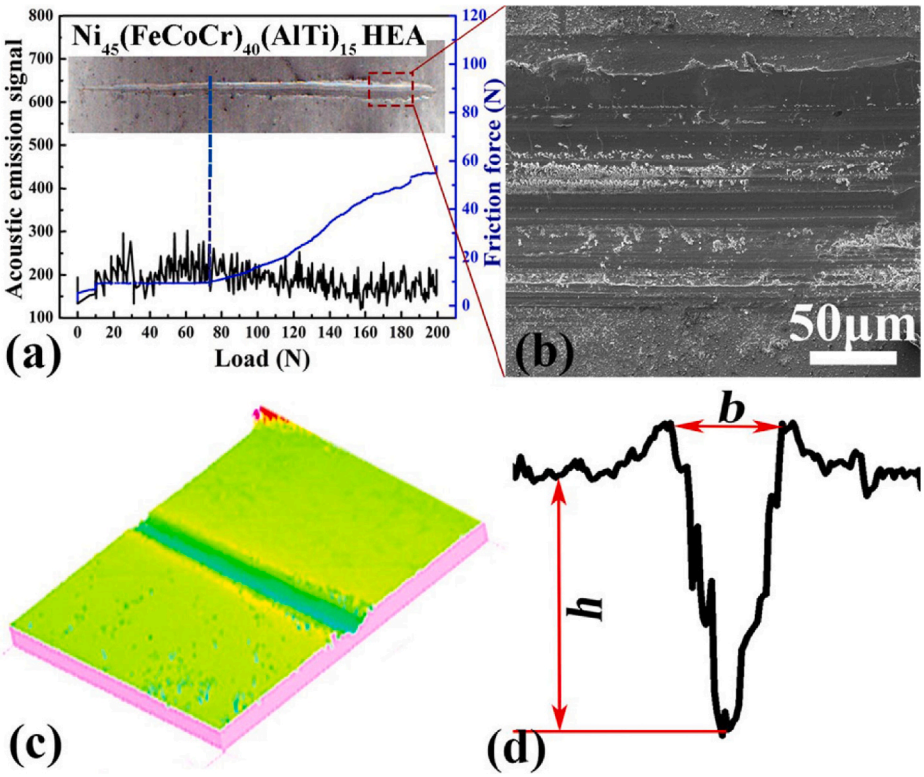

Fig. 5. The scratch test of the nitrided layer: (a) The scratch acoustic-emission signal and friction curve; (b) The morphology of the largest deformation of the scratch; The 3D topography (c) and 2D contour (d) of the scratch at a load of 72 N.

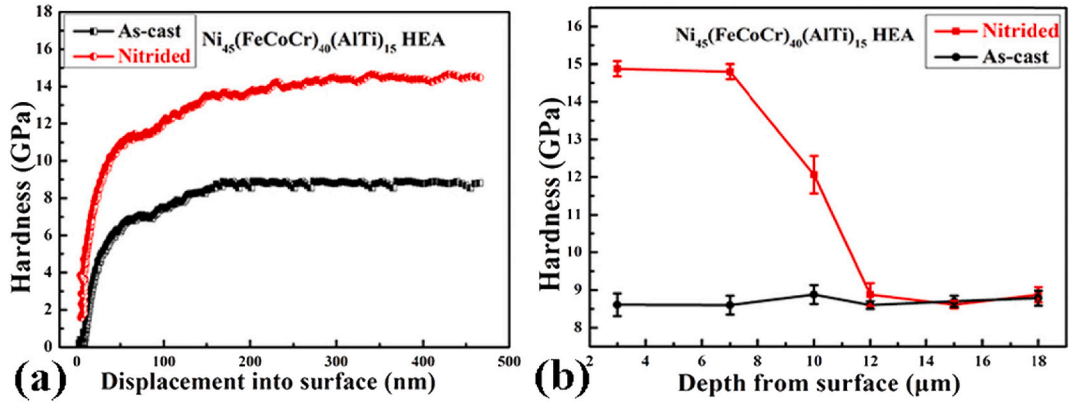

Fig. 6. (A) The nano-hardness of the as-cast and nitrided $Ni_{45}(FeCoCr)_{40}(AlTi)_{15}$ HEAs surfaces. (b) The hardness-depth profiles for as-cast and nitrided HEAs.

have the same tendency. The friction coefficient gradually rises to a stable value and periodically fluctuates within a small range with the damage and compaction of the wear scar surface, which is called the transition from the running-in stage to stable stage. Another similar feature is that the friction coefficient of as-cast and nitrided HEAs has the same variation trend with increasing the temperature. The friction coefficient increases first and then decreases. However, the friction coefficient of the as-cast alloy increases gradually within 20–200 °C and then decreases gradually, while the friction coefficient of the nitrided alloy reaches the maximum at 300 °C due to the different sensitivities of the as-cast and nitrided alloy surfaces to frictional heat, resulting in different formation rates of the oxide film during the friction process.

The coefficient of friction of the nitrided alloy is lower than that of the as-cast alloy at the same temperature, as listed in Table 3. The surface structures of nitrided alloys are different from those of as-cast alloys, as reflected in Fig. 3(b). During the wear test of nitrided alloys, the Si_3N_4 pellet scratched with the surface nitrides first. As described above, the surface of the nitrided alloy was composed of a plurality of nitride phases, and the nanoscale nitride particles were uniformly distributed on the FCC substrate to enhance the entire compound layer. These nanoscale particles were difficult to ground and decompose due to the high hardness, meaning that numerous balls were added between the friction pairs. The existence of the ball changed the wear mechanism from the sliding friction to rolling friction on a microscopic scale. Meanwhile, due to the rolling of the hard nanoparticles, it was easier to smash the abrasive debris generated between the friction pairs, reducing the abrasive wear and the fluctuation of the friction coefficient caused by the friction debris as the third body.

3.2.2. *Worn surface and wear mechanism*

Fig. 8 shows the wear-surface morphologies of as-cast HEAs at different temperatures. There are many grooves parallel to the sliding

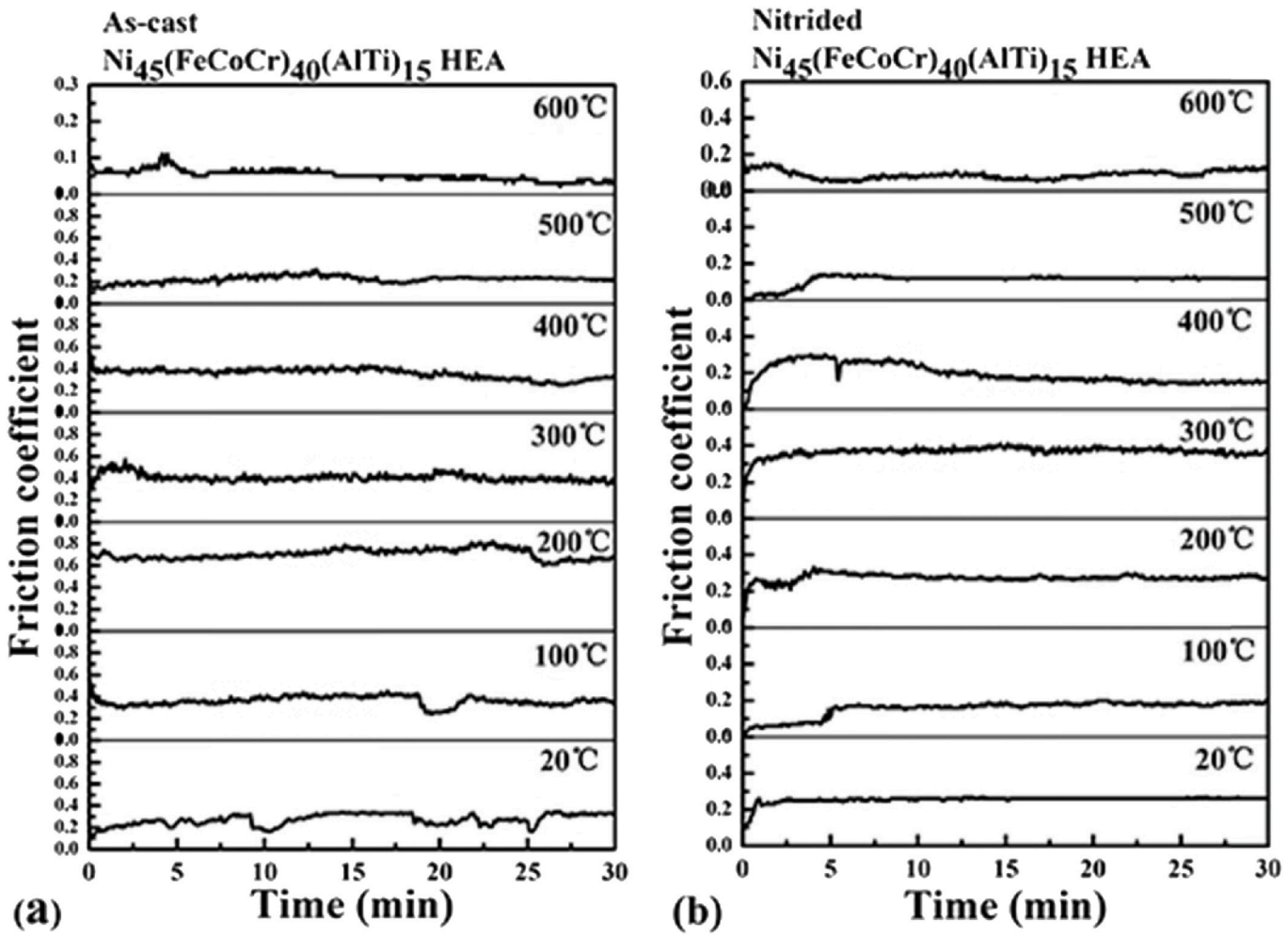

Fig. 7. Friction coefficient as a function of the sliding time for $Ni_{45}(FeCoCr)_{40}(AlTi)_{15}$ HEAs: (a) as-cast alloys, (b) nitride alloys.

Table 3
The friction coefficients of as-cast and nitrided $Ni_{45}(FeCoCr)_{40}(AlTi)_{15}$ alloys at different temperatures.

	20 °C	100 °C	200 °C	300 °C	400 °C	500 °C	600 °C
as-cast	0.32 ± 0.02	0.36 ± 0.02	0.69 ± 0.03	0.38 ± 0.03	0.33 ± 0.02	0.21 ± 0.01	0.12 ± 0.01
nitrided	0.2 ± 0.01	0.26 ± 0.01	0.27 ± 0.02	0.35 ± 0.02	0.15 ± 0.01	0.13 ± 0.01	0.12 ± 0.02

direction, and some granular and flake-like debris as seen in Fig. 8(a), (b), (c), and (d), which is the typical feature of the abrasive wear. Moreover, more debris is observed on the wear surface as shown in Fig. 8 (c). In addition, Fig. 8 (c) shows that the grooves scratched by the abrasive grains are deeper and wider compared to the wear surface of the as-cast HEAs at 20 and 100 °C as shown in Fig. 8(a) and (b). Hence, more severe abrasive wear occurred at 200 °C, which was consistent with the results of the friction coefficient in Fig. 7. The oxygen content of the wear debris of as-cast HEAs at different temperatures reflected from Table 4 is much higher than that of the surface, indicating the occurrence of the debris-oxidation reaction. Furthermore, the loose particles and plastic deformation areas of the worn surface imply the characteristics of the adhesive wear. Plastic shearing of the surface of the asperity contact resulted in the peeling of the worn debris. Due to the adhesion effect, the debris generated by the sliding may adhere to the worn surface and transfer to the Si_3N_4, or to other previously-attached fragment to form larger agglomerate, which was easily oxidized due to its large surface area, reducing the adhesion strength of the debris [36,37]. Therefore, the debris was peeled off from the surface, forming loose particles. Some of the debris was ground and drawn at the cyclic stress, and sintered at high temperatures to form the deformation areas as reflected in Fig. 8(b). Therefore, the dominant wear mechanisms of as-cast alloys from 20 to 300 °C were abrasive wear and adhesive wear of the oxidized particles.

The surface morphology is smoother, and only some tiny debris and shallow scratches are observed with no large grooves and fragments at 400 °C and 500 °C as shown in Fig. 8 (e) and (f), indicating the slight abrasive wear. Therefore, the friction coefficient was decreased. The oxygen content on the worn surface and debris is higher as shown in Table 3, suggesting a mechanism of the oxidative wear. Furthermore, irregularly-shaped pits are traces of brittle oxide-film peeling, which is also a feature of the oxidative-wear mechanism. The adhesion effect is weakened due to the formation of the thick oxide film, which acts as a solid lubricant to avoid the direct contact of the friction pairs. The presence of the flake structure and the cracks indicates that the delamination wear has occurred at 400 °C as exhibited in Fig. 8(e). The asperity on the soft surface was subjected to cyclic loading, and the shear plastic deformation occurred and accumulated in the surface layer, leading to the periodic dislocations in the metal surface layer. According to the Hertz-contact theory [38], the dislocation density near the surface

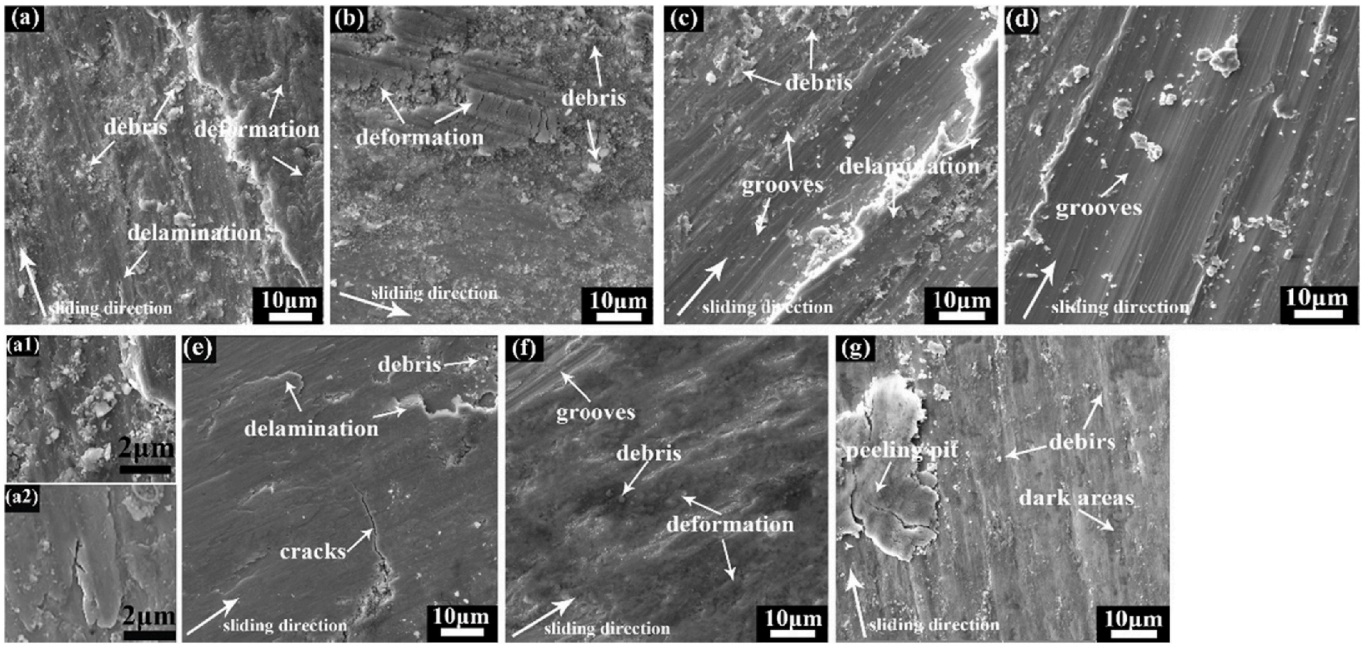

Fig. 8. SEM images of the worn surfaces of as-cast $Ni_{45}(CoCrFe)_{40}(AlTi)_{15}$ HEAs at different temperatures: (a) 20 °C; (b) 100 °C; (c) 200 °C; (d) 300 °C; (e) 400 °C; (f) 500 °C; and (g) 600 °C; (a1) and (a2) are the magnification images of debris and delamination in Fig. 8 (a).

Table 4
Chemical compositions (at. %) of the wear debris and worn surfaces of $Ni_{45}(CoCrFe)_{40}(AlTi)_{15}$ HEAs at different temperatures.

Temperature		Al	Co	Cr	Fe	Ni	Ti	O
20 °C	Debris	6.2	9.8	9.4	9.8	31.1	5.8	27.9
	Surface	6.8	12.0	11.7	11.5	38.3	6.6	13.0
100 °C	Debris	3.5	5.9	5.9	5.8	19.3	3.5	55.9
	Surface	6.6	12.8	12.4	12.6	42.0	7.7	5.9
200 °C	Debris	7.4	8.7	8.8	8.8	29.0	5.3	31.9
	Surface	7.5	12.7	12.4	12.0	40.2	7.0	8.2
300 °C	Debris	6.9	7.0	7.1	6.9	22.2	3.9	46.0
	Surface	7.8	12.6	12.4	11.8	42.9	9.6	2.8
400 °C	Debris	4.1	6.0	6.2	5.9	19.9	3.6	54.4
	Surface	3.8	6.6	6.6	6.2	20.5	3.7	52.7
500 °C	Debris	5.1	4.4	5.8	4.4	15.0	3.2	62.1
	Surface	3.3	6.0	6.1	5.7	19.0	3.7	56.2
600 °C	Debris	3.5	4.9	5.1	5.1	16.1	3.0	62.3
	Surface	2.0	6.2	4.5	9.4	14.4	2.5	60.9

was lower than that inside, indicating that the maximum shear deformation occurred within a certain depth. During the friction process, the shear deformation accumulated, causing the dislocation accumulation at a certain depth below the surface, which resulted in the formation of cracks or holes. According to the stress-field analysis, the normal stress on the parallel surface prevented the crack from extending in the depth direction, but extended in the direction parallel to the surface. When the crack propagated to a critical length, the material between the crack and the surface was peeled off in the form of the flaky debris [39]. The hardness of the alloy decreased slightly with the temperature further increasing to 600 °C. Moreover, the delamination wear occurred on the contact surface, forming the flake debris, as exhibited in Fig. 8(g). Therefore, the wear mechanism at high temperatures was mainly oxidative and delamination wear.

The overall wear-surface morphology of the nitrided HEAs is much smoother than that of the as-cast HEAs, as shown in Fig. 9. The surface hardness of the nitrided alloy was significantly increased. The nanohardness was increased from 8.8 GPa for the as-cast HEAs to 14.9 GPa for the nitrided HEAs, which means that a higher ultimate shear strength needs to be overcome in the process of sliding. Hence, it is difficult to produce large debris to plough the surface and form large grooves under the same conditions [40]. However, a small amount of tiny debris and slight scratches indicate that the slight abrasive wear has occurred. The black areas in Fig. 9(a), (b), and (c) indicate the characteristics of the adhesive wear. The elastic deformation of the friction-pair contact decreases due to the higher hardness of the material surface, which means that the contact area of the friction pair decreases, and the contact pressure increases. It is easier to form bonding points at the contact interface. As a result, the characteristics of the adhesive wear are more prominent [41]. However, the area of the dark region decreases significantly with increasing the temperature, which means that the degree of adhesive wear is decreased. The adhesive wear is the most serious at room temperature. However, small amounts of tiny debris and fine scratches reflect the characteristics of slight abrasive wear [14].

The wear surface of the nitrided $Ni_{45}(CoCrFe)_{40}(AlTi)_{15}$ HEAs changes greatly with the temperature increasing to 300 °C. The disappearance of the plastic deformation and dark areas indicates that the adhesive wear has not occurred (Fig. 9 (d)). The smooth wear surface and a large number of small and irregular debris of the nitrided $Ni_{45}(CoCrFe)_{40}(AlTi)_{15}$ HEAs indicate the occurrence of the oxidative wear. Moreover, the spalling of oxide particles increases the wear-surface roughness, increasing the friction coefficients of the nitrided HEAs at 300 °C, as reflected in Fig. 6 and Table 3.

Some delamination fractures are detected in Fig. 9(e). Friction is a process of energy consumption. In addition to the frictional heat, the friction energy was partially consumed to form the wear debris. When the energy accumulated to the critical value, the fragments were generated and even peeled off. The fracture of the brittle material was caused by the normal stress. The hard and brittle oxide film was destroyed by friction for a long time, thus forming the delamination structure and leading to the occurrence of delamination wear. The smoother surface morphology with the scattered tiny debris and small scratches is presented in Fig. 9(f) and (g). The complete oxide film is more protective for the wear surface during sliding.

3.2.3. *Wear rate*

Fig. 10(a) reflects the wear rates of the as-cast and nitrided $Ni_{45}(CoCrFe)_{40}(AlTi)_{15}$ HEAs specimens at different temperatures. It is found that the wear rate of the nitrided alloys drops sharply compared with

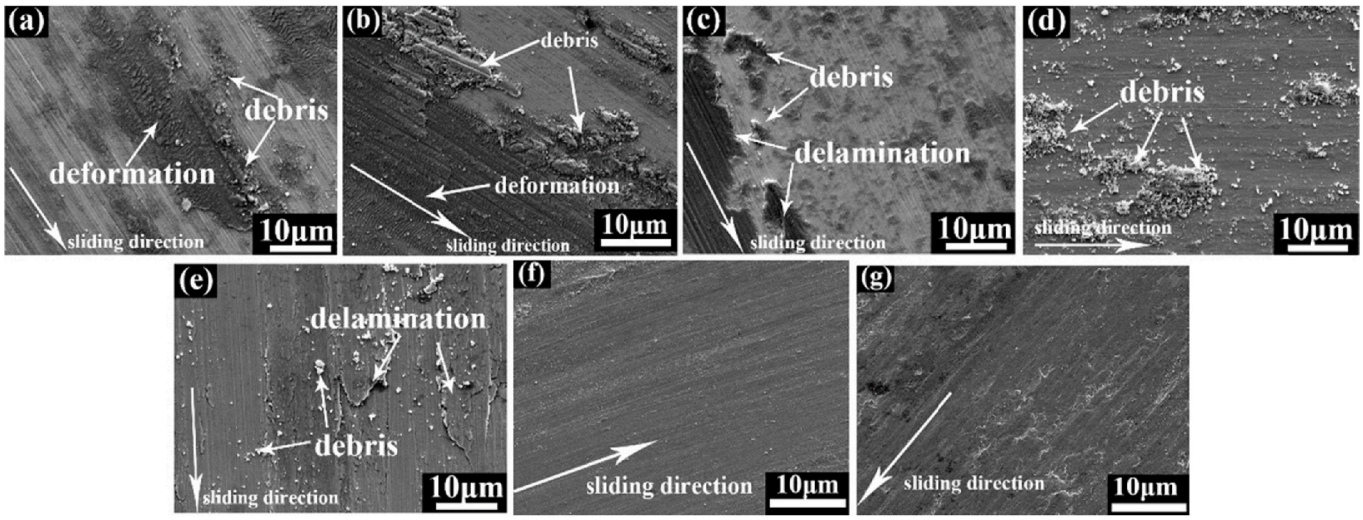

Fig. 9. SEM images of the worn surfaces of nitrided $Ni_{45}(CoCrFe)_{40}(AlTi)_{15}$ HEAs at different temperatures: (a) 20 °C; (b) 100 °C; (c) 200 °C; (d) 300 °C; (e) 400 °C; (f) 500 °C; and (g) 600 °C.

that of the as-cast alloys in accordance with the Archard's law, that is, the wear resistance of the alloy is proportional to the hardness [42]. The maximum wear rate of the nitrided alloy is 8×10^{-5} mm^3/(Nm) at 20 °C, which is much lower than the minimum wear rate of the as-cast alloy at 300 °C [23×10^{-5} mm^3/(Nm)]. The hardness reflects the ability of the material to resist the intrusion of the material into the surface [43]. The high hardness results in shallow scratches on the surface, and the volume of the wear scar generated by the cutting is minute, that is, the wear resistance is high. It is found that the minimum volume loss of the as-cast alloy is 1.01 mm in width and 24 μm in depth, while the maximum volume loss of the nitrided alloy is 0.63 mm in width and 9.7 μm in depth, which indicates that the volume loss of the nitrided samples is much lower than that of the as-cast alloys. Moreover, the nitrided layer was not worn through during wear (the thickness of the nitrided layer was 11.5 μm).

Combined with Figs. 7(a), 8 and 10(a), the trend of the wear rate of the as-cast alloy was consistent with the analysis of the friction coefficient and wear morphology. The friction coefficient and wear rate of the as-cast alloy are higher at 200 °C than those at other temperatures. XPS was used to analyze the chemical valence and strength of oxygen elements on the wear surface of the as-cast alloy at different temperatures, as presented in Fig. 11. The oxygen peaks become increasingly stronger with the increase of temperature, indicating that the degree of oxidation increases.

The wear rate of the nitrided alloy can be divided into three stages as a function of temperature. First, from 20 to 200 °C, the wear rate decreases with increasing the temperature due to the reduced adhesion

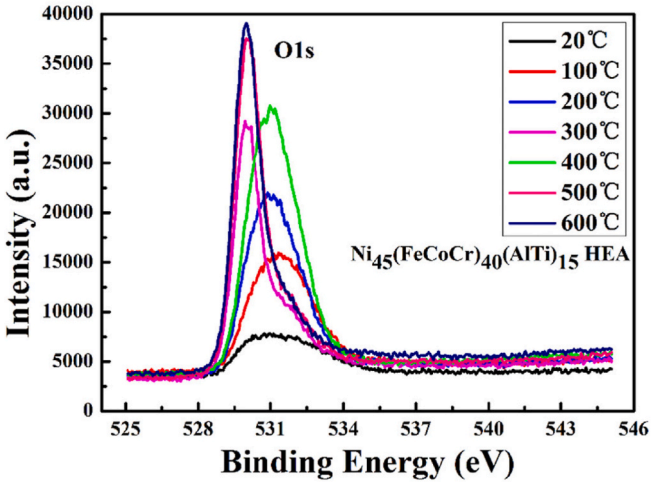

Fig. 11. The chemical valence and strength of oxygen elements on the wear surfaces of as-cast alloys at different temperatures.

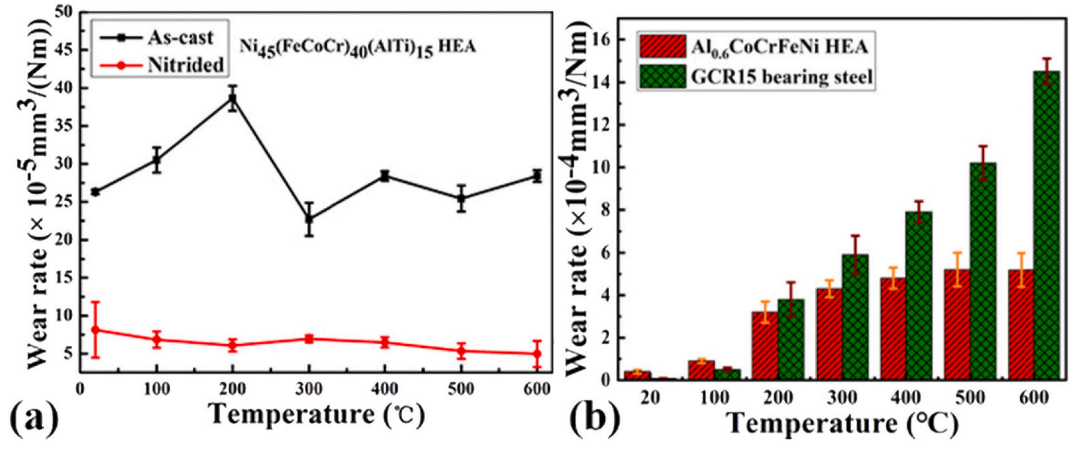

Fig. 10. Wear rates of (a) as-cast and nitrided $Ni_{45}(CoCrFe)_{40}(AlTi)_{15}$ HEAs; (b) $Al_{0.6}CoCrFeNi$ and GCr15 bearing steel at different temperatures.

effect. The above analysis has confirmed that the wear mechanism at this stage is mainly abrasive and adhesive wear. However, the surface was not softened with increasing the temperature due to the high-temperature resistance of the nitrided layer. Hence, the wear particles have limited the damage to the surface. Furthermore, the protection of the oxide film and high temperature reduced the bonding strength at the nanoscale between the friction-pair contact surfaces as shown in Fig. 9 (a)–(c). Hence, the total wear loss was actually weakened, and the wear rate was reduced.

From 200 to 300 °C, the wear rate increases slightly due to the variation of friction mechanism as reflected in Fig. 10(a). The large amount of particles and the friction coefficient suggest the instability of the friction process, indicating that the formation and removal of the oxide film compete with each other. Moreover, the continuous peeling and formation of the oxide film lead to an increase of the wear rate.

The decrease of the wear rate in the third stage (as reflected in Fig. 10 a) is mainly attributed to the anti-wear and protective effect of the oxide film. The smooth friction coefficient indicated that the friction process is stable at this stage, as exhibited in Fig. 7, and the oxidation rate is higher than the wear rate. The elemental composition and chemical state of the $Ni_{45}(CoCrFe)_{40}(AlTi)_{15}$ HEA oxide film analyzed at 600 °C by XPS are presented in Fig. 12. The main components of alloys oxide films are Al_2O_3, Cr_2O_3, and Fe_2O_3, among which Al_2O_3 and Cr_2O_3 have dense structures and strong adhesion. Thus, the protective film formed is very dense, reducing the diffusion rate of O ions and thereby preventing the continuous oxidation of the substrate. Accordingly, this feature ensures the excellent oxidation resistance of the $Ni_{45}(CoCrFe)_{40}(AlTi)_{15}$ alloys at high temperatures [44].

Fig. 12(g) shows the curve-fitted N 1s spectrum of nitrides dispersed on the worn surface. The main N 1s peaks of TiN are 396.7 eV and 397.17 eV. The electron binding energy peak of N and Al is about 396.20 eV, which corresponds to Al2p3/2 (the binding energy peak appears at 74.40 eV), indicating the formation of AlN compounds. Furthermore, combined with the analysis of the XPS detection results of Fe, Cr and N, it is concluded that Fe_3N and CrN were formed during the nitriding process, and the corresponding binding energies of N1s peaks are 396.80 eV and 397.30 eV, respectively.

The friction and wear experiments of $Al_{0.6}CoCrFeNi$ HEAs and GCr15 were carried out in the previous experiments [14]. Moreover, the test and calculation methods were completely consistent with those of $Ni_{45}(CoCrFe)_{40}(AlTi)_{15}$ HEAs in this paper. The wear rate of as-cast $Ni_{45}(CoCrFe)_{40}(AlTi)_{15}$ alloys is higher than that of $Al_{0.6}CoCrFeNi$ HEAs and GCr15 bearing steel at lower temperature (≤200 °C) as indicated in Fig. 10. The wear rate of $Ni_{45}(CoCrFe)_{40}(AlTi)_{15}$ alloys decreases above 300 °C, while the wear rates of $Al_{0.6}CoCrFeNi$ HEAs and GCr15 bearing steel continue to increase with increasing the temperature, and the wear rate of $Ni_{45}(CoCrFe)_{40}(AlTi)_{15}$ alloys is significantly lower than that of other two. Especially, at 600 °C, the wear rate of GCr15 is higher 5 times than that of the as-cast $Ni_{45}(CoCrFe)_{40}(AlTi)_{15}$ alloys and 29 times than that of the nitrided $Ni_{45}(CoCrFe)_{40}(AlTi)_{15}$ alloys, which indicates that the $Ni_{45}(CoCrFe)_{40}(AlTi)_{15}$ alloys have higher wear resistance. Some studies have shown that the carbide phase is easily decomposed at high temperatures, decreasing the hardness of GCr15 rapidly [45,46]. However, the high-entropy alloys have higher resistance to high-temperature softening. According to Archard's law [32], the wear resistance of the alloy is directly proportional to the hardness. Therefore, the wear rate is different greatly at high temperatures.

4. Discussion

4.1. The formation of nitride phases

AlN, CrN, Fe_3N, and TiN phases are formed after nitriding, as shown in Fig. 2. The studies have shown that the lower formation enthalpy means that the compound has a higher bond energy and better stability [35,47]. For example, the enthalpies of formation of some nitrides were AlN (− 318 kJ/mol), CrN (− 125 kJ/mol), Fe_3N (− 2.2 kJ/mol), and Ni_3N (+ 0.2 kJ/mol), indicating that N elements tend to combine with Al, Cr, and Fe to form nitrides under the same conditions, while it is difficult to generate Ni_3N. Moreover, the diffraction peak of Ni_3N is not observed in the XRD pattern in accordance with the thermodynamic-analysis results. The higher hardness of the nitrided alloy can be attributed to the inherent hardness of the deposited compounds, that is, the hardness of the nitride phase is much higher than that of the matrix, which is different from the high hardness of the coating due to the presence of nanocrystalline phase in previous studies [48].

Compared with the as-cast alloys, the increase in hardness of nitrided alloys can be attributed to (1) the dispersion strengthening of a large number of nitrides, since the total percentage of strong and moderate nitriding forms, such as Al, Cr, Fe, and Ti, is 41.7 at.%, and (2) the strengthening effect of nitrogen atoms on the solid solution in the non-nitride phase of the nitrided layer [47].

4.2. Effect of temperature on friction coefficient

Fig. 7 shows the influence of temperature on the friction coefficient of as-cast and nitrided HEAs. The friction coefficient of both of them increases first and then decreases with the increase of temperature, but the turning points are different. The friction coefficients of the as-cast alloys turn at 200 °C, while that of the nitrided alloys reach their maximum at 300 °C. During the sliding process, most of the frictional energy is consumed by plastic deformation, which is directly converted into the thermal energy of the surface material. The contact between two bodies can be approximated as a single contact or as multiple contacts [49]. Friction changes the chemical-reaction dynamics between the friction pairs, resulting in reactions that need to be carried out at high temperatures and that can occur at room temperature during sliding. Such reactions induced by the friction energy are referred to as tribochemistry reactions, and the wear controlled by this reaction is called as the tribochemical wear [50,51]. In the case of the low stress contact, the asperity interaction results in instantaneous high temperatures, and thermal oxidation triggered by temperature rise promotes the formation of surface oxide film, which is generally considered as a beneficial form of corrosion [52]. At low temperatures, oxidation occurs at the convex contact of the surface due to the frictional heat, while at higher temperatures, oxidation occurs on the entire surface and changes the wear mechanism [52,53]. Oxygen molecules bind to metal atoms on the surface of the fresh metal and form strong chemical bonds. This oxidation product prevents further diffusion of oxygen molecules, inhibiting the persistence of chemical bonds [54]. The oxidation of many metals follows the following rules [55].

$$h = Ct^{1/2} \tag{3}$$

where h represents the thickness of oxide film, t is the growth time, and C is the constant of parabolic rate.

In addition, because the frictional heat excites molecular diffusion, the growth rate of the oxide-film thickness during sliding is also a function of temperature [55]:

$$K = A\exp(-Q/RT) \tag{4}$$

where K is the growth-rate constant of the oxide film, A is the chemical reaction constant [$kg^2/(m^4\ s)$], Q is the activation energy associated with the oxidation reaction (kJ/mol), R is the gas constant, and T is the thermodynamic temperature of the surface. During the formation of the oxide film, two competing processes occur: the breakdown of the oxide film leads to the formation of further debris particles, and the oxidation reaction of the fresh metal to form the oxide film [14]. The formation or removal of such layers depends on the dominant party in the competition. The contact of the asperities results in adhesive contacts caused by

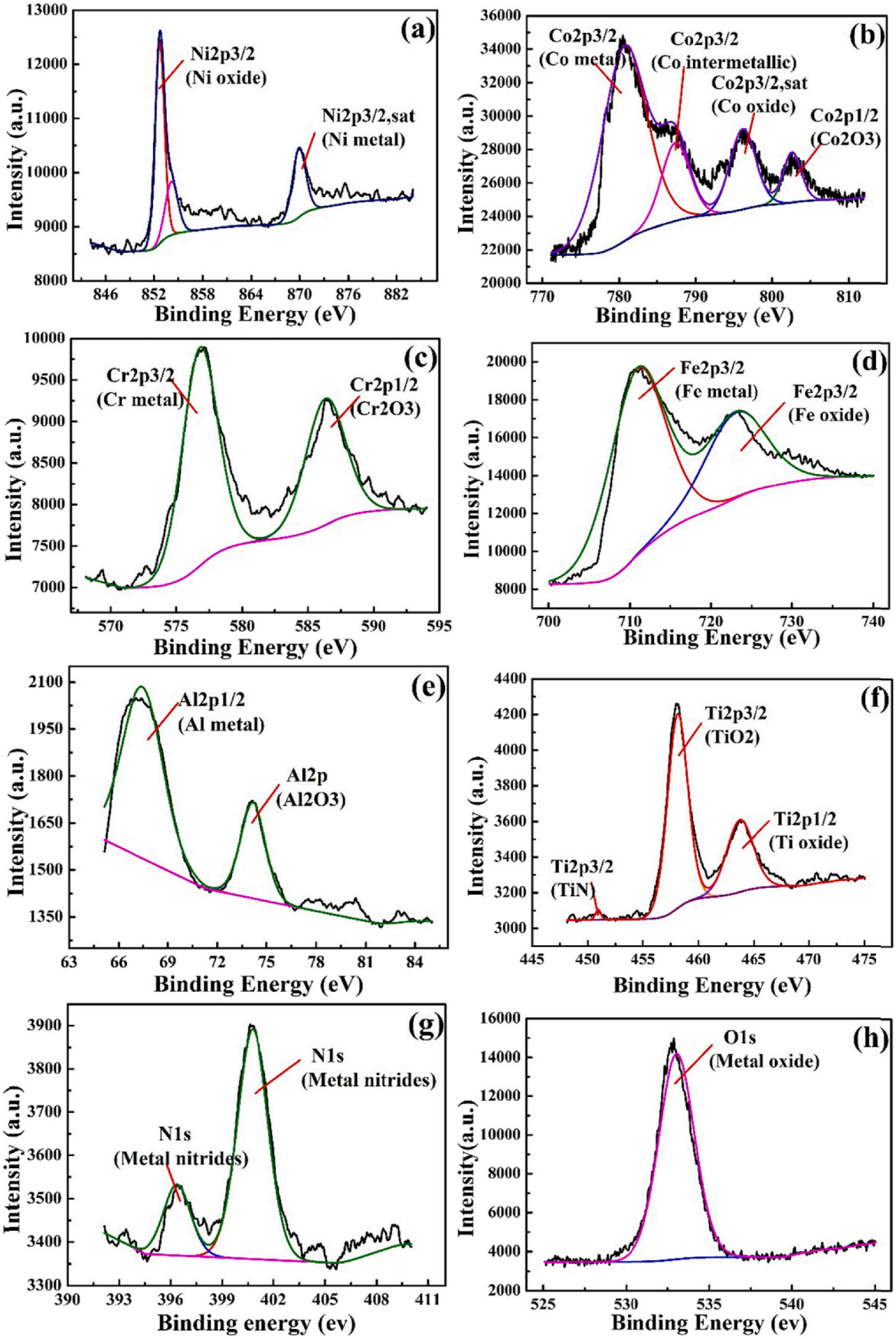

Fig. 12. XPS analysis of the oxidation films of nitrided alloys tested at 600 °C: (a) Ni element; (b) Co element; (c) Cr element; (d) Fe element; (e) Al element; (f) Ti element; (g) N element; and (h) O element.

interatomic interactions. The friction force is contributed by the adhesion of the asperities and other sources of surface interactions during relative sliding. A lateral force is required to shear the adhesive bonds, and after shearing of the existing contacts, new contacts are formed, which is an important factor for increasing the friction coefficient. According to Eqs. (3) and (4), the growth rate of the oxide film is slow at a lower temperature, forming the thin oxide film. The oxide film ruptured under the action of cyclic pressure, forming the granular or flaky fragments. Subsequently, the metal exposed to the environment was further oxidized to form a new oxide film. The formation and destruction of the oxide film were a repeated process, and the accumulation of debris increased the roughness of the worn surface. The ambient temperature gradually increased from 20 °C to 200 °C, the as-cast alloys gradually thickened the oxide film generated due to the friction heat, but the oxide-film removal speed was still higher than the formation speed, generating more debris and increasing the friction coefficient as reflected in Fig. 8. Meanwhile, the increase in the amount of debris causes more adhesive contacts on the wear surface and improves the friction force. At higher ambient temperatures, the oxide generated by the external environment and the sliding process may be partially or completely removed due to the sliding effect, so the oxide film will gradually thicken. The oxide film adhered to the surface of the wear scar and separated the Si_3N_4 ball from the fresh metal surface instead of directly contacting it. In addition, the oxide film can be used as a smooth bearing zone and can be regarded as a solid lubricant to reduce the friction coefficient by taking advantage of its lower shear stress and higher hardness. Meanwhile, the temperature has a great influence on the adhesion. When the contact-interface temperature is higher than the critical value, the adhesion decreases with the increase of temperature [56,57]. Therefore, the friction coefficient decreases with the ambient temperature increasing from 300 to 600 °C. However, the nitrides produced on the surface of the nitrided HEAs had good thermal stability and high dispersion, leading to the higher atmospheric corrosion resistance and temperature softening resistance of the nitride layer and reducing the notch sensitivity [34,35]. Therefore, the change of the friction coefficient of the nitrided alloy occurs at 300 °C, which is summarized in Fig. 7 and Table 3.

4.3. Effect of temperature on wear rate of as-cast alloy

Combined with Figs. 7(a), 8 and 10(a), the friction coefficient and wear rate of the as-cast alloy at 200 °Care higher than those at other temperatures. The XPS analysis results indicate that the oxidation rate increases with the increase of temperature, as shown in Fig. 11. Detailed studies have shown that changes in the wear scars were related to the formation of the compaction layer of oxide fragments and some oxide particles on the sliding surface, and most of the retained particles participated in the development of the compact layers [58,59]. During the cyclic sliding process, the agglomerated particles were subjected to the thermoelastic stress and compaction, while the fine particles were more likely to stick together when heated. The sintering rate of particles increases with increasing the temperature, and the oxidation rate of the residual metal in the particles increased, which formed sturdier and smooth solid layers [58,60,61]. These layers provided long-lasting protection because the oxide debris was further formed after decomposition and re-compacted to the smooth surface. Thus, following the establishment of the wear debris layers, two competing processes occurred during sliding. If the compacted layer was hard enough not to be scratched, the smooth solid layer can effectively protect the surface and reduce the wear rate. On the contrary, if the fragments and sintered particles were insufficiently compacted, it was easier to produce loose abrasive particles to damage the surface, resulting in an increased wear rate.

Moreover, assuming that the wear volume of the compacted layer is negligible and only debris particles are further generated from the original alloys contact surface of the sliding part, which is justified, because the wear volume loss mainly came from the scratching of the soft surface by the wear debris. The volume of the pear groove formed by the injury was lost, and the harder compacted layer was not easily scratched as reflected in Figs. 8 and 9. Therefore, the volume of the worn debris particles remaining on the sliding surface after sliding can be expressed as [39]:

$$\mathrm{Vr}\ (\mathrm{t}) = \frac{\pi}{6}\int_0^t \left\{ AN(t)[1-C_e(t)] \int_0^\infty \left[D^3 f(D)(1-P_r(D))\right] dD \right\} dt \tag{5}$$

where A is the obvious area of the wear scar at that time; $N(t)$ is the number of wear debris particles formed at unit time; $C_e(t)$ is the effective coverage of the wear protective layers at that time; $f(D)\mathrm{d}D$ is the percentage of newly formed particles that fall within the diameter range; $P_r(D)$ is the probability that a wear particle is removed from the wear track, and D is the diameter.

Assuming that all the remaining debris particles are finally merged into a wear debris layer with an average thickness d, the coverage of these layers on the area of apparent wear marks is [35]]:

$$C_{comp} = \frac{V_r(t)}{2Ad} \tag{6}$$

Formulae (3) and (4) describe in detail the kinetic model followed in the formation of the oxide layer. If an oxide 'glaze' of a critical thickness can be established on its surface, the wear debris particle layer is particularly effective in preventing wear.

Assuming that a compacted wear debris layer area, $dA_c(\tau)$, was formed at time, τ, a "glazed" area will be formed after a while, and the total area of "glazed" at time, t, is given by Ref. [35]:

$$A_g(t) = \int_0^{t-t(c)} dA_c(\tau) \tag{7}$$

where t(c) is the critical time for a 'glaze' of critical thickness to develop on the compacted debris.

Thus, it is obvious that the compacted clastic particles and oxidized "glaze" layers can coexist on sliding surfaces. Although both types are protective, the "glaze" layer is more effective. Therefore, the production of a higher coverage, thicker and denser oxide layer at high temperature can better protect the surface of the material, reducing the wear rate (Fig. 10 a), and resulting in a transition from severe wear to slight wear (Figs. 8 and 9).

5. Conclusions

In the present work, $Ni_{45}(FeCoCr)_{40}(AlTi)_{15}$ HEAs were prepared by arc melting with a water-cooled copper mold, and then the nitrided layers were prepared by plasma nitriding. The microstructures of the as-cast and nitrided alloys, the properties of the nitrided layer, and the influence of temperature on the friction coefficient, wear rate and friction mechanism of different samples was investigated. The following conclusions are drawn:

(1) The XRD results reflected that as-cast $Ni_{45}(FeCoCr)_{40}(AlTi)_{15}$ HEAs consisted of single FCC phases. The FCC peak intensity of the nitrided alloy dropped sharply, and the hard phases of AlN, CrN, Fe_3N, and TiN appeared. The surface roughness increased from 6.3 nm in the as-cast alloys to 97.7 nm in the nitrided alloys.
(2) The surface hardness of the alloy increased from 8.8 GPa in the as-cast material to 14.9 GPa in the nitrided alloy. The thickness of the nitrided layer was about 11.5 μm. The hardness of the nitrided layer was uniform at different depths and the nitride layer had a good bonding strength with the substrate.
(3) Compared with the as-cast alloy, the improvement of the surface hardness and the formation of nitrided particles effectively reduced the friction coefficient. The friction coefficient of the as-

cast alloy increased gradually from 20 °C to 200 °C, and then decreased gradually until 600 °C. The change of the friction coefficient of the nitrided alloy appeared at 300 °C. Further, the coefficient of friction was slightly different in all cases.

(4) The wear resistance of the nitrided alloy was higher than that of the as-cast alloy at higher temperatures, and both of them had lower wear rates at high temperatures due to the protection and anti-wear effect of oxide films.

(5) The wear mechanism of as-cast and nitrided alloys was mainly dominated by the abrasive and adhesive wear at lower temperatures, and gradually changed to the oxidative and delamination wear with increasing the temperature.

6. Data availability statement

The raw/processed data required to reproduce these findings cannot be shared at this time due to technical or time limitations.

Credit Author Statement

L.W. Lan: Formal analysis, Investigation, Writing – original draft, H. J. Yang: Writing – review & editing, Supervision, Project administration, R.P. Guo: Methodology, X.J. Wang: Validation, M. Zhang: Resources, P. K. Liaw: Data curation, J.W. Qiao: Conceptualization, Visualization

Declaration of competing interest

We solemnly declare that we fully own the copyright of the manuscript and do not infringe the rights and interests of others. We declare that we have no known competing financial interests or personal relationships that could have appeared to influence the work reported in this paper. We confirm that the manuscript has been read and approved by all named authors and that there are no other persons who satisfied the criteria for authorship but are not listed. We further confirm that the order of authors listed in the manuscript has been approved by all of us. We guarantee that the content of this manuscript has not previously been protected or published by copyright. We promise that the content of this manuscript will not be copyrighted, submitted or published elsewhere.

Acknowledgements

The authors would like to acknowledge the financial support of the Natural Science Foundation of Shanxi Province, China (Nos. 201901D111105 and 201901D111114), Transformation of Scientific and Technological Achievements Programs of Higher Education Institutions in Shanxi (2019), and the opening project of State Key Laboratory of Explosion Science and Technology (Beijing Institute of Technology), and the opening project number is KFJJ20-13M. PKL very much appreciates the supports from (1) the National Science Foundation (DMR-1611180 and 1809640) with the program directors, Drs. Judith Yang, Gary Shiflet, and Diana Farkas and (2) the Army Office Project (W911NF-13-1-0438 and W911NF-19-2-0049) with the program managers, Michael P. Bakas, David M. Stepp, and S. Mathaudhu.

References

[1] J.W. Yeh, S.K. Chen, S.J. Lin, J.Y. Gan, T.S. Chin, T.T. Shun, et al., Nanostructured high-entropy alloys with multiple principal elements: novel alloy design concepts and outcomes, Adv. Eng. Mater. 6 (2004) 299–303.

[2] Senkov ON, Scott JM, Senkova SV, Miracle DB, Woodward CF. Microstructure and room temperature properties of a high-entropy TaNbHfZrTi alloy. J. Alloys Compd.;509:0-6048.

[3] K.M. Youssef, A.J. Zaddach, C. Niu, D.L. Irving, C.C. Koch, A novel low-density, high-hardness, high-entropy alloy with close-packed single-phase nanocrystalline structures, Materials Research Letters 2 (2014), 1.

[4] S. Yoshida, T. Bhattacharjee, Y. Bai, N. Tsuji, Friction stress and Hall-Petch relationship in CoCrNi equi-atomic medium entropy alloy processed by severe plastic deformation and subsequent annealing, Scripta Mater. 134 (2017), 33.

[5] K.Y. Tsai, M.H. Tsai, J.W. Yeh, Sluggish diffusion in Co–Cr–Fe–Mn–Ni high-entropy alloys, Acta Mater. 61 (2013) 4887–4897.

[6] O.N. Starovoytov, M. Gao, S. Guo, E. Khosravi, J. Lei, L. Tan, et al., Comparative studies of the ground state properties for Nb25Mo25Ta25W25 and V20Nb20Mo20Ta20W20, TMS2013 Supplemental Proceedings (2013) 1137–1145.

[7] M.J. Jang, S. Praveen, H.J. Sung, J.W. Bae, J. Moon, H.S. Kim, High-temperature tensile deformation behavior of hot rolled CrMnFeCoNi high-entropy alloy, J. Alloys Compd. 730 (2018) 242–248.

[8] M. Bulletin, Wear-resistant boride nanocomposite coating exhibits low friction, MRS Bull. 34 (2009), 792.

[9] Senkov ON, Wilks GB, Miracle DB, Chuang CP, Liaw PK. Refractory high-entropy alloys. Intermetallics;18:0-1765.

[10] W.H. Liu, Y. Wu, J.Y. He, T.G. Nieh, Z.P. Lu, Grain growth and the Hall–Petch relationship in a high-entropy FeCrNiCoMn alloy, Scripta Mater. 68 (2013) 526–529.

[11] M.R. Chen, S.J. Lin, J.W. Yeh, M.H. Chuang, S.K. Chen, Y.S. Huang, Effect of vanadium addition on the microstructure, hardness, and wear resistance of Al 0.5 CoCrCuFeNi high-entropy alloy, Metall. Mater. Trans. Part A 37 (2006) 1363–1369.

[12] M.H. Chuang, M.H. Tsai, W.R. Wang, S.J. Lin, J.W. Yeh, Microstructure and wear behavior of Al x Co 1.5 CrFeNi 1.5 Ti y high-entropy alloys, Acta Mater. 59 (2011) 6308–6317.

[13] X. Lin, Z. Bai, Y. Liu, B. Tang, H. Yang, Sliding tribological characteristics of in-situ dendrite-reinforced Zr-based metallic glass matrix composites in the acid rain, J. Alloys Compd. 686 (2016) 866–873.

[14] M. Chen, L. Lan, X. Shi, H. Yang, M. Zhang, J. Qiao, The tribological properties of Al0.6CoCrFeNi high-entropy alloy with the σ phase precipitation at elevated temperature, J. Alloys Compd. 777 (2019) 180–189.

[15] Y. Wang, Y. Yang, H. Yang, M. Zhang, S. Ma, J. Qiao, Microstructure and wear properties of nitrided AlCoCrFeNi high-entropy alloy, Mater. Chem. Phys. 210 (2018) 233–239.

[16] Y. Wang, Z. Zhou, Improvement of impact wear performance of Ti6Al4V alloy by nitrogen ion implantation and nitriding, China Mech. Eng. 21 (2010) 1214–1217.

[17] B-l Jiang, J-m Li, H-y Shi, L-j Bai, Application of microarc oxidation Technology in magnesium alloy protective treatment [J], Automobile Technology & Material 5 (2003) 24–27.

[18] L.Y. Zhang, L.I. Jun, L. Zuo, B.J. Liu, J. Peng, Comparison and analysis of the surface roughness of galvannealed automobile outer panel produced domestically and abroad, J. Mater. Metall. 4 (3) (2005) 245–248.

[19] J.X. Hou, J. Fan, H.J. Yang, Z. Wang, J.W. Qiao, Deformation behavior and plastic instability of boronized Al 0.25 CoCrFeNi high-entropy alloys, International Journal of Minerals, Metallurgy and Materials 27 (2020) 1363–1370.

[20] E.N. Eremin, S.A. Guchenko, V.C. Laurynas, V.M. Yurov, S.S. Kasymov, Laser alloying of nanocrystalline coatings, J. Phys. Conf. 1210 (1) (2019), 012038.

[21] Lampke Thomas, Löbel Martin, Sattler Benjamin, Surface hardening of FCC phase high-entropy alloy system by powder-pack boriding, Surf. Coating. Technol. 371 (2019) 389–394.

[22] J. Jiang, F.H. Stott, M.M. Stack, The role of triboparticulates in dry sliding wear, Tribol. Int. 31 (12) (1998) 245–256.

[23] O.E. Okorafor, Fracture toughness of M2 and H13 alloy tool steels, Metal Science Journal 3 (1987) 118–124.

[24] Wang J, Xiong J, Peng Q, Fan H, Wang Y, Li G, et al. Effects of DC plasma nitriding parameters on microstructure and properties of 304L stainless steel. Mater. Char.; 60:197-203.

[25] Huang HH, He JL, Hon MH. Microstructure and mechanical properties of surface layer obtained by plasma nitriding and/or TiN coating on high speed steel. Surf. Coating. Technol.;64:41-46.

[26] A. Nishimoto, T. Fukube, T. Maruyama, Microstructural, mechanical, and corrosion properties of plasma-nitrided CoCrFeMnNi high-entropy alloys, Surf. Coating. Technol. 376 (2019) 52–58.

[27] Y. Wang, Y. Yang, H. Yang, M. Zhang, S. Ma, J. Qiao, Microstructure and wear properties of nitrided AlCoCrFeNi high-entropy alloy, Mater. Chem. Phys. 210 (2018) 233–239.

[28] X.F. Wang, Y. Zhang, Y. Qiao, G.L. Chen, Novel microstructure and properties of multicomponent CoCrCuFeNiTix alloys, Intermetallics 15 (2007) 357–362.

[29] C.W. Lin, M.H. Tsai, C.W. Tsai, J.W. Yeh, S.K. Chen, Microstructure and aging behaviour of Al5Cr32Fe35Ni22Ti6 high entropy alloy, Mater. Sci. Technol. 31 (2015), 1165.

[30] L. Zhang, Y. Zhou, X. Jin, X. Du, B. Li, The microstructure and high-temperature properties of novel nano precipitation-hardened face centered cubic high-entropy superalloys, Scripta Mater. 146 (2018) 226–230.

[31] C.W. Lin, M.H. Tsai, C.W. Tsai, J.W. Yeh, S.K. Chen, Microstructure and aging behaviour of Al5Cr32Fe35Ni22Ti6 high entropy alloy, Mater. Sci. Technol. 31 (2015), 1165.

[32] M. Chen, X.H. Shi, H. Yang, P.K. Liaw, M.C. Gao, J.A. Hawk, et al., Wear behavior of Al0.6CoCrFeNi high-entropy alloys: effect of environments, J. Mater. Res. 33 (2018) 3310–3320.

[33] Q. Wang, Z. Lei, J. Dong, Effects of plasma nitriding on microstructure and tribological properties of CoCrMo alloy implant materials, JBE 7 (2010) 337–344.

[34] T.H. Hsieh, C.H. Hsu, C.Y. Wu, J.Y. Kao, C.Y. Hsu, Effects of deposition parameters on the structure and mechanical properties of high-entropy alloy nitride films[J], Curr. Appl. Phys. 18 (5) (2018) 512–518.

[35] T.H. Hsieh, C.H. Hsu, C.Y. Wu, et al., Effects of deposition parameters on the structure and mechanical properties of high-entropy alloy nitride films, Curr. Appl. Phys.: the official journal of the Korean Physical Society 18 (2018) 512–518.
[36] T. Miyajima, Y. Iwai, Effects of reinforcements on sliding wear behavior of aluminum matrix composites, Wear 255 (2003) 606–616.
[37] A. Chiba, K. Kumagai, N. Nomura, S. Miyakawa, Pin-on-disk wear behavior in a like-on-like configuration in a biological environment of high carbon cast and low carbon forged Co–29Cr–6Mo alloys, Acta Mater. 55 (2007) 1309–1318.
[38] Savkoor AR, Briggs GAD. The effect of tangential force on the contact of elastic solids in adhesion. Proc. Roy. Soc. Lond.;356:103-114.
[39] F.H. Stott, High-temperature sliding wear of metals, Tribol. Int. 35 (2002) 489–495.
[40] L. Du, L. Lan, S. Zhu, H. Yang, X. Shi, P. Liaw, et al., Effects of temperature on the tribological behavior of Al0. 25CoCrFeNi high-entropy alloy, J. Mater. Sci. Technol. 35 (2019) 917–925.
[41] J. Hou, M. Zhang, H. Yang, J. Qiao, Y. Wu, Surface strengthening in Al0. 25CoCrFeNi high-entropy alloy by boronizing, Mater. Lett. 238 (2019) 258–260.
[42] W.U. Hong, I. Baker, Y. Liu, W.U. Xiao-Lan, Dry sliding tribological behavior of Zr-based bulk metallic glass, Trans. Nonferrous Metals Soc. China 22 (2012) 585–589.
[43] K. Herrmann, Hardness Testing: Principles and Applications, ASM international, 2011.
[44] Bala N, Singh H, Prakash S. High-temperature oxidation studies of cold-sprayed Ni–20Cr and Ni–50Cr coatings on SAE 213-T22 boiler steel. Appl. Surf. Sci.;255: 6862-6869.
[45] Serna MM, Rossi JL. Mc Complex carbide in aisi M2 high-speed steel. Mater. Lett.; 63:p.691-693.
[46] S. Varalakshmi, M. Kamaraj, B.S. Murty, Processing and properties of nanocrystalline CuNiCoZnAlTi high entropy alloys by mechanical alloying, Mater. Sci. Eng., A 527 (2010) 1027–1030.
[47] None, in: F.G. Walton Smith (Ed.), Handbook of Marine Science, 1, CRC Press, Cleveland, Ohio, 1974, 640 pp. Price $43.95.Ecological Aspects of Toxicity Testing of Oils and Dispersants. Edited by L. R. Beynon and E. B. Cowell Barking, Essex: Applied Scienc. Journal of the Marine Biological Association of the United Kingdom;55:507.
[48] M.L. Kuruppu, G. Negrea, I.P. Ivanov, S.L. Rohde, Monolithic and multilayer Cr/CrN, Cr/Cr2N, and Cr2N/CrN coatings on hard and soft substrates, Journal of Vacuum Science & Technology A Vacuum Surfaces & Films 16 (1998) 1949–1955.
[49] Liu YJ, Li SJ, Wang HL, Hou WT, Hao YL, Yang R, et al. Microstructure, defects and mechanical behavior of beta-type titanium porous structures manufactured by electron beam melting and selective laser melting. Acta Mater.;113:56-67.
[50] T.E. Fischer, M.P. Anderson, S. Jahanmir, R. Salher, Friction and wear of tough and brittle zirconia in nitrogen, air, water, hexadecane and hexadecane containing stearic acid ☆, Wear 124 (1988) 133–148.
[51] T. Egami, Y. Waseda, Atomic size effect on the formability of metallic glasses, J. Non-Cryst. Solids 64 (1984) 113–134.
[52] T.F.J. Quinn, Review of oxidational wear Part II: recent developments and future trends in oxidational wear research, Tribol. Int. 16 (1983) 305–315.
[53] Höpfner W. Handbook of Corrosion Data. second ed., hrsg. von Bruce D. Craig und David S. Anderson, ASM International Materials Park, OH 44073, Juni 1995, 998 S., $ 188,–, ISBN 0-87170-518-4. In Europa zu beziehen durch: American Technical Publishers Ltd., 27. Materials & Corrosion 1996;47.
[54] R.A. Bagnold, Experiments on gravity-free dispersion of large solid spheres in a Newtonian fluid under shear, Procroysoclondon 225 (1954) 49–63.
[55] P.K. Sharma, L. Bhushan, J.K. Ladha, R.K. Naresh, R.K. Gupta, B. V. Balasubramanian, et al., Crop-water relations in rice-wheat cropping under different tillage systems and water-management practices in a marginally sodic, medium-textured soil 8 (2002) 223–235.
[56] A. Gåård, N. Hallbäck, P. Krakhmalev, J. Bergström, Temperature Effects on Adhesive Wear in Dry Sliding Contacts, vol. 268, 2010, pp. 968–975.
[57] H. Engqvist, N. Axén, Abrasion of Cemented Carbides by Small Grits, vol. 32, 1999, pp. 527–534.
[58] F. Stott, High-temperature sliding wear of metals, Tribol. Int. 35 (2002) 489–495.
[59] M. Qiu, Y. Zhang, J. Yang, et al., Effects of friction heat on tribological properties of Ti6Al4V alloy sliding against GCr15 steel[J], TRIBOLOGY-BEIJING- 26 (3) (2006), 203.
[60] H. Itoh, K. Saitoh, K. Nagata, Evaluation of sliding wear properties of metals and coating at high temperature, Nihon Kikai Gakkai Ronbunshu, A Hen/Transactions of the Japan Society of Mechanical Engineers 68 (Part A) (2002) 1389–1394.
[61] Y. Liu, H. Wang, Microstructure and high-temperature sliding wear property of Coss/Co3Mo2Si metal silicide alloys, Mater. Sci. Eng., A 396 (2005) 240–250.